

EXTENT OF EXCESS FAR INFRARED EMISSION AROUND LUMINOSITY CLASS III STARS

SUNGSOO S. KIM, B. ZUCKERMAN, & MURRAY SILVERSTONE¹

Division of Astronomy & Astrophysics, University of California, Los Angeles, CA 90095-1562;
sskim@astro.ucla.edu, ben@astro.ucla.edu, murray@as.arizona.edu

To appear in the Astrophysical Journal, March 20, 2001 issue

ABSTRACT

With the *Infrared Space Observatory*, we conducted 3×3 -pixel imaging photometry of twelve luminosity class III stars, which were previously presumed to have dust particles around them, at far infrared wavelengths (60 and $90 \mu\text{m}$). Eleven out of twelve targets show a peak of excess (above photosphere) far infrared emission at the location of the star, implying that the dust particles are truly associated with stars. To estimate the size of the excess emission source, the flux ratio of center to boundary pixels of the 3×3 array was examined. The radius of the dust emission is found to be ~ 3000 to ~ 10000 AU for a thin shell distribution, and ~ 5000 to ~ 25000 AU for a uniform distribution. We consider three models for the origin of the dust: disintegration of comets, sporadic dust ejection from the star, and emission from nearby interstellar cirrus. The data seem to rule out the first model (as far as the “Kuiper–belt” like particles are assumed to be large blackbody grains), but do not enable us to choose between the other two models.

Subject headings: stars: late-type — circumstellar matter — infrared: stars

1. INTRODUCTION

Zuckerman, Kim, & Liu (1995) correlated the Bright Star Catalog (Hoffleit & Warren 1991) and the Michigan Spectral Catalog (Houk, Cowley, & Smith-Moore 1975–1988) with the IRAS catalogs to determine which, if any, luminosity class III giant stars (first ascent red giants) have associated circumstellar dust particles that radiate at far infrared (far-IR) wavelengths. Of more than 40,000 class III giant stars in the two catalogs, they found that perhaps 300 have associated dust.

Whereas the presence of particulate material near pre-main sequence, main-sequence, AGB, and supergiant stars may be accounted for in rather straightforward ways (remnants from the star formation for the former two, and mass loss for the latter two), there is no obvious way to produce and retain large amounts of dust near first ascent giant stars, which are thought to be too old to still possess much left-over material and insufficiently evolved to have lost a significant amount of their mass. However, one may conjecture that the presence of dust around first ascent giants may involve one or more of the following phenomena: mass loss, binarity, planetary systems, and evaporation of Kuiper–belt material. Recently, Jura (1999) has analysed three models for the dust around eight first ascent giant stars: orbiting dust resulting from the disintegration of comets located in extrasolar analogs of the Kuiper belt, dust sporadically ejected from the star, and emission from particles in the interstellar medium which are accidentally near the star, the “cirrus hotspot”.

Among the Zuckerman et al. (1995) list of 300, we observed 12 first ascent giant stars with the PHOT instrument of the *Infrared Space Observatory* (*ISO*²) to determine if the excess far-IR emission is truly associated with the stars and to estimate the size of the region that produces the excess far-IR emission.

§ 2 describes our *ISO* observations and data reduction. § 3 discusses the data analysis including the determination of the size of the far-IR excess source. § 4 then compares our results

with Jura’s models. A summary is given in § 5.

2. OBSERVATIONS & DATA REDUCTION

The target stars were observed with the C100 camera of the ISOPHOT instrument using filters 60 ($\lambda_c = 60.8 \mu\text{m}$, $\Delta\lambda = 23.9 \mu\text{m}$) and 90 ($\lambda_c = 95.1 \mu\text{m}$, $\Delta\lambda = 51.4 \mu\text{m}$). C100 is a 3×3 Ge:Ga pixel array. The sky coverage of each pixel is $43.5'' \times 43.5''$ and the gap between adjacent pixels corresponds to $2.5''$ on the sky. The diffraction limit of the ISO is $25''$ at $60 \mu\text{m}$ and $38''$ at $90 \mu\text{m}$. Observation mode PHT37–39 was used to obtain a sequence of dark–off1–on–off2 measurements for each target and filter. The target was measured at the on sequence position and, to obtain the background intensity around the target, two off-position measurements (off1 & off2) were made at a single position $2.5'$ closer to the nearer celestial pole than the target. Calibration measurements were performed at the dark and off2 sequence positions using the Fine Calibration Source 1 (FCS1) onboard the satellite. The integration time was 64 s for scientific measurements (target and background) and 32 s for FCS1 measurements.

The data were reduced using the PHOT Interactive Analysis software package (PIA, Gabriel et al. 1997) version 7.2.2(e). Each measurement consisted of 64 ramps (16 for FCS1), and each ramp has 31 non-destructive readouts (63 for FCS1) and 1 destructive readout. Data reductions described below used the default values of the PIA except when specified. Non-linearity correction and two-threshold deglitching were applied to each ramp, and a linear-fit was made to the ramp to derive the signals in V/s. These signals were deglitched again using the minmax clipping algorithm with a threshold set at 2.4σ . Then reset interval correction and dark current subtraction were applied to the signals.

The responsivity of the system, that is the conversion of signal (V/s) to flux (Jy), was obtained by time-interpolating two FCS1 measurements for each target. At each star the background at each of the nine pixels was obtained from an average

¹Present address: Steward Observatory, University of Arizona, Tucson, AZ 85721

²*ISO* is an ESA project with instruments funded by ESA member states (especially the PI countries: France, Germany, The Netherlands and the United Kingdom) and with the participation of ISAS and NASA

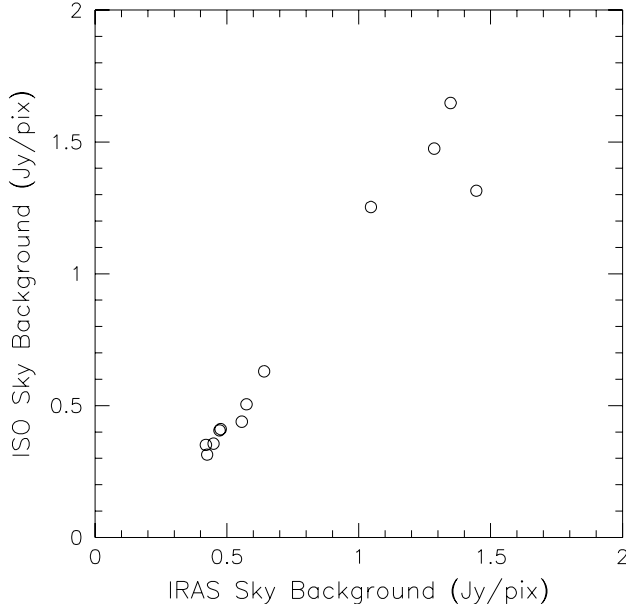


FIG. 1.— Comparison of $60\ \mu\text{m}$ background flux observed by the *IRAS* and *ISO* near our target stars. Fluxes are in units of Jy per one ISO C100 pixel area. IRAS flux is the 4' IRAS Sky Survey Atlas background before subtraction of a zodiacal model. The mean of the difference between two data sets is 0.4 %, and the standard deviation of the mean of the difference is 5 %. The uncertainty in flux ranges from 2.2 to 4.8 % for the ISO data, and from 0.1 to 4.6 % for the IRAS data (the IRAS uncertainty is from the cirrus confusion noise).

of the *off1* and *off2* images. Inspection of the $60\ \mu\text{m}$ background fluxes obtained in this way at the 12 target stars indicated a larger flux (by 10%) at the central pixel of the background; this difference between central and boundary pixels is larger than the spatial variation of the background. We interpret the difference as due to a bias in the FCS1 signal and correct for it as follows. The flux of each *on* pixel is divided by the background flux of the corresponding pixel and multiplied by the average of the 9 pixel background flux. This background average is then subtracted from the *on* pixel flux to produce a measure of the source flux.

To check the accuracy of data measurement and reduction, our ISO background average and the 4' IRAS Sky Survey Atlas background (before the subtraction of a zodiacal model) were compared. Figure 1 shows that the two flux values agree very well.

The uncertainty for the background flux was estimated by taking the rms value of the 9 differences between 2 *off* measurements of each pixel. The uncertainty for the total boundary-pixel flux of the source was estimated to be the square-root of 4 times the sum of the variance of 4 crossing pixels and that of 4 diagonal pixels considering the point-symmetric nature of the Point Spread Function (PSF). Since only 1 pixel measurement is available for the central pixel of the source, we simply assume that background and central *on*-pixel uncertainties are proportional to their fluxes. The average signal-to-noise ratio (S/N) is found to be ~ 20 for background flux and ~ 5 for central flux of the source, and ~ 2.2 for boundary-pixel flux of the source. However, our analysis involves the boundary-pixel flux of the source only in the context of a sum of 8 boundary-pixel fluxes, which has an average S/N of ~ 6 .

Measured ISO fluxes are presented in Table 1 along with the IRAS fluxes. Since the fluxes are neither color-corrected, nor compensated for their detector sizes and PSF shapes, the ISO and IRAS data are not to be compared directly.

3.1. Association with Optical Counterparts

Since the presumed optical counterparts are targeted at the central pixel of the 3×3 array, if the material responsible for excess far-IR emission is distributed around the star with an intensity concentration toward the center or with an extent smaller than one pixel size, the intensity of the central pixel in our ISO data should be highest. We find that the peak intensity is located at the central pixel for all stars except HD 221776 which has $90\ \mu\text{m}$ peak intensity at the boundary pixel to the south, and HD 24124 that has 60 and $90\ \mu\text{m}$ peak intensities at the boundary pixel to the northwest. We have identified in the Digitized Sky Survey a galaxy-like object at the location of the 60 and $90\ \mu\text{m}$ peak intensities of HD 24124. Since the peak intensity pixels at both passbands coincide with the nearby galaxy, we attribute to it the far-IR emission previously presumed to be associated with HD 24124. However, in the case of HD 221776, because no object was found near the position of $90\ \mu\text{m}$ peak intensity from the Digitized Sky Survey, and because the $60\ \mu\text{m}$ peak intensity occurs at the central pixel, we believe that the $60\ \mu\text{m}$ peak intensity is truly associated with the star and the $90\ \mu\text{m}$ peak intensity is not real or is due to an unidentified nearby object. In addition, the second brightest $90\ \mu\text{m}$ pixel is the central one and the ratio of 60 to $90\ \mu\text{m}$ fluxes is plausible for a real source located at the star.

The fact that the central pixel has the highest intensity for 11 out of 12 stars at $60\ \mu\text{m}$ suggests that the far-IR IRAS sources truly are associated with most of the giant stars presented in Table 1 of Zuckerman et al. (1995).

TABLE 1
ISO AND IRAS FLUXES (JY)

Star	$F_{\text{ISO}}(60\mu\text{m})$			$F_{\text{ISO}}(90\mu\text{m})$			F_{IRAS}		
	center (pixel)	boundary (pixel sum)	background (average)	center (pixel)	boundary (pixel sum)	background (average)	12 μm	25 μm	60 μm
HD 119853	0.289 ± 0.089	0.509 ± 0.185	1.315 ± 0.059	0.187 ± 0.071	0.229 ± 0.229	1.047 ± 0.049	2.360	0.571	0.887
HD 221776	0.271 ± 0.045	0.293 ± 0.095	0.630 ± 0.025	0.177 ± 0.061	0.813 ± 0.112	0.691 ± 0.049	5.080	1.360	0.840
HD 153687	1.288 ± 0.127	1.543 ± 0.414	1.253 ± 0.069	0.755 ± 0.103	0.669 ± 0.478	1.349 ± 0.053	13.700	4.160	5.120
HD 156115	0.265 ± 0.107	0.225 ± 0.194	1.648 ± 0.071	0.221 ± 0.103	0.351 ± 0.191	1.786 ± 0.060	8.900	2.280	0.913
HD 202418	0.305 ± 0.036	0.477 ± 0.135	0.411 ± 0.019	0.218 ± 0.040	0.444 ± 0.173	0.558 ± 0.022	2.400	0.696	0.919
HD 218559	0.157 ± 0.036	0.320 ± 0.073	0.406 ± 0.028	0.107 ± 0.030	0.280 ± 0.066	0.482 ± 0.018	3.570	0.977	0.580
HD 212320	0.172 ± 0.083	0.221 ± 0.080	1.475 ± 0.045	0.180 ± 0.062	0.436 ± 0.109	1.007 ± 0.037	1.300	0.422	0.606
HD 19745	0.255 ± 0.034	0.133 ± 0.083	0.314 ± 0.025	0.220 ± 0.030	-0.034 ± 0.054	0.298 ± 0.020	0.296	0.777	0.612
HD 24124	0.000 ± 0.025	0.145 ± 0.114	0.351 ± 0.021	0.034 ± 0.021	0.352 ± 0.293	0.283 ± 0.016	0.334	0.250	0.400
HD 111830	0.395 ± 0.044	0.127 ± 0.100	0.505 ± 0.022	0.337 ± 0.058	0.398 ± 0.170	0.776 ± 0.034	0.571	0.231	0.972
HD 92253	0.158 ± 0.032	0.137 ± 0.062	0.439 ± 0.019	0.139 ± 0.049	0.198 ± 0.117	0.770 ± 0.031	0.774	0.223	0.604
HD 32440	0.237 ± 0.033	0.155 ± 0.095	0.356 ± 0.021	0.154 ± 0.027	0.073 ± 0.076	0.444 ± 0.011	8.000	2.000	0.573

NOTE.— Fluxes are non-color corrected. Central-pixel and sum of boundary-pixel fluxes are listed in the second and third, and fifth and sixth column for the 60 and 90 μm images, respectively. The background intensity, in an average background pixel, that was subtracted from the on-source fluxes is given in columns four and seven. The IRAS 12, 25 and 60 μm source fluxes are from the Faint Source Catalog. The boundary pixel to the south in the HD 221776 90 μm source image, which has the out-of-center peak intensity, was not considered when deriving its boundary-pixel flux.

A 3×3 array is too coarse to give information on the source size directly from its image. However, if the distribution of the emission source is simple and axisymmetric about the image center, the extent of the source may be inferred from the ratio (r) of the flux in the central pixel to the sum of the fluxes in the 8 boundary pixels (Table 1). When defining r , only excess (i.e., non-photospheric) emission is considered. By comparing the measured flux ratio r_{obs} and a model flux ratio r_{mod} , one may estimate the size of the extended source.

When calculating r_{mod} , one first needs a footprint, which is the fraction of the energy in the PSF that falls onto a pixel as a function of the pixel's location relative to the center of the PSF. Then the fraction of the flux onto a certain pixel from an extended emission source is obtained by convolving the footprint with an assumed source distribution. The PIA package includes model footprints of the ISOPHOT C100 camera, but a recent footprint calibration (Laureijs 1999) shows that the observed footprints for the whole array at a few different locations are slightly smaller than the PIA model values. While the PIA model gives the full 2-dimensional footprint, the calibration by Laureijs gives footprint values only at few locations in the focal plane. Thus one has to modify the PIA model footprint so that it best matches the Laureijs calibration. We find that shrinking the x-y scale (focal plane scale) of the model PIA footprint by 15 % can well fit the observed footprint values. We choose altering the x-y scale of the model footprint instead of dividing all footprint values by a certain constant because the former also gives good fits to the ratios of observed footprints while the latter does not.

Here we assume two simple models for the distribution of the material responsible for excess far-IR emission: 1) an infinitesimally thin shell around the central star with an angular radius of θ_{ex} , appropriate for the orbiting and ejected circumstellar dust models, and 2) uniform distribution of material cen-

tered on the star with an angular radius of θ_{ex} , appropriate for the cirrus hotspot model (see § 1 and Jura 1999 for a detailed description of the orbiting dust, ejected dust, and cirrus hotspot models). Then r_{mod} is a ratio of the footprint convolved with the assumed distribution with a given θ_{ex} for central pixel (f_c) to that for the sum of the boundary pixels (f_b):

$$r_{\text{mod}}(\theta_{\text{ex}}) \equiv \frac{f_c(\theta_{\text{ex}})}{f_b(\theta_{\text{ex}})}. \quad (1)$$

For the shell distribution model, the footprint is convolved with the projected distribution of a shell of constant intensity. In the case of a uniform distribution, the footprint is convolved with the projected distribution of a filled dust sphere with a radial intensity profile appropriate for optically thin, equilibrium approximation³. The calculated $r_{\text{mod}}(\theta_{\text{ex}})$ is presented in Figure 2.

The observed fluxes also include a contribution from the photosphere of the central star. Following Jura (1999), we estimate the photospheric emission from the star at 60 μm using the IRAS 12 μm flux and an assumed photospheric ratio $F^*(60)/F^*(12)$ of 0.0371 (Jura obtained this value by averaging the IRAS colors of the 9 brightest K and G giants in the Yale Bright Star Catalog). When converting the estimated IRAS photospheric flux for the ISO filters, we adopt color-correction factors for a 4000 K blackbody. The 90 μm photospheric flux is extrapolated from the 60 μm photosphere with a blackbody assumption. The photosphere emission at 60 and 90 μm is assumed to be not diluted by the presence of a circumstellar shell. The estimated photospheric fluxes are given in Table 2. The contribution of the central star to the flux in each pixel can then be determined from the footprint and we subtract these photospheric fluxes from the observed fluxes to determine r_{obs} :

$$r_{\text{obs}} \equiv \frac{F_c - P_c F^*}{F_b - P_b F^*}, \quad (2)$$

³See Appendix B of Sopka et al. 1985 for the radial intensity profile. The intensity profile is basically a Planck function with a local temperature given by their equation [B3], which is proportional to $R^{-2/(4+p)}$ where R is the radius from the star and p is the emissivity index. We adopt $p = 1.5$ following Jura 1999 and assume that the photospheric emission from the central star follows a Planck function as well.

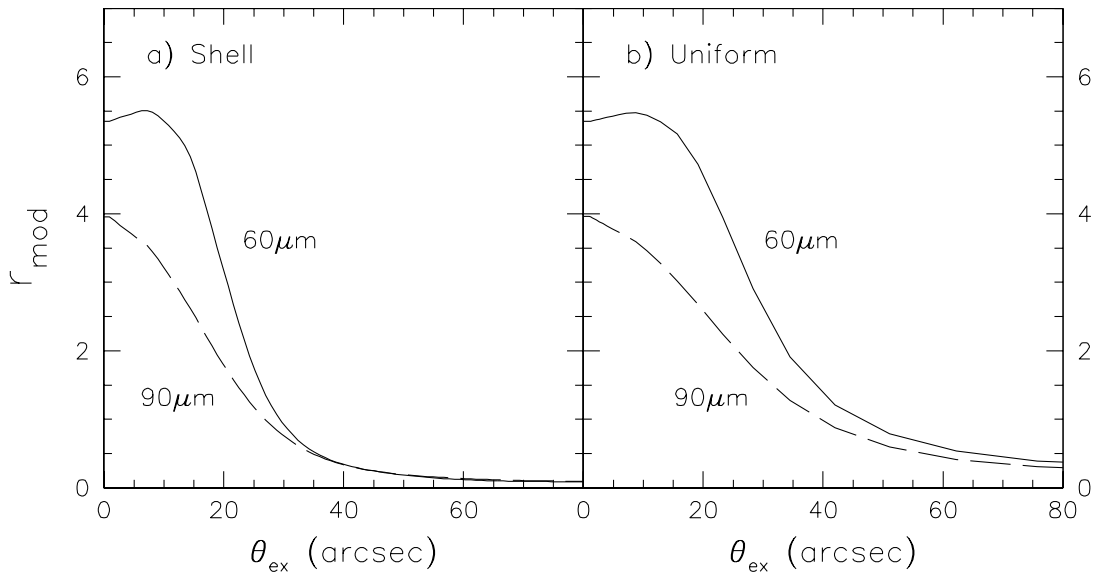


FIG. 2.— Modelled intensity ratio of central to boundary pixels of the ISO C100 camera, r_{mod} , for the extended, excess far-IR emission source at 60 (solid lines) and 90 μm (dashed lines). *a*) For an infinitesimally thin shell of circumstellar matter with an angular radius of θ_{ex} . *b*) For a uniform distribution of cirrus material with an angular radius of θ_{ex} . In case of the latter, the intensity ratio is a function of central star’s parameters, D_* , T_* , and R_* . The intensity ratio shown in *b*) is for HD 119853. r_{mod} has an initial rise near $\theta_{ex} = 0''$ at 60 μm , whose existence is a result of the detailed shape of the footprint.

where F is the observed source flux, F^* is the estimated photospheric flux, P is the fraction of the flux that falls onto the central pixel or boundary pixels from a point source located at the center of the array, and the subscripts c and b are for the center and boundary pixels, respectively. P_c and P_b values, adopted from the modified PIA footprint model, are 0.66 & 0.12 for 60 μm , and 0.59 & 0.15 for 90 μm , respectively (the rest of the flux falls outside the array). The variables for the boundary pixels are summed over the eight pixels.

The angular size of the extended emission source, θ_{ex} , can be obtained from equating r_{mod} and r_{obs} . We find θ_{ex} that satisfy $r_{mod}(\theta_{ex}) = r_{obs}$ for both a shell and a uniform source distribution. The size of the extended emission source, R_{ex} , then follows from this θ_{ex} and the Hipparcos measured distance to the star, D_* (see Table 4). Derived R_{ex} values and their uncertainties for our targets are given in Table 3 as well as r_{obs} .

The θ_{ex} values found here for the shell distribution (see Table 3) range from 20'' to 40'' (30'' to 70'' for the uniform distribution), implying that we were able to deconvolve extended sources whose angular size is smaller than the 43'' 1 pixel size of the detector. Plets et al. (1997), whose work was similar to that of Zuckerman et al. (1995), state that most of their luminosity class III giants with excess far infrared emission appear to be unresolved in IRAS scans at 60 μm . We have convolved the 60 μm IRAS PSF with the projected distribution of a shell with an angular radius of 30'', which is the typical angular size of extended emission sources derived in the present study, and found that the full-width-half-maximum of the convolved distribution was only $\sim 15\%$ larger than that of the PSF. This small difference is thought to be the reason that the sources in Plets et al. “look” unresolved. By deconvolving the PSF, Hawkins & Zuckerman (1991) were able to resolve some objects with an angular radius smaller than 30'' at 60 μm , but their objects mostly had relatively high fluxes (larger than a few Jy).

Since our targets have fluxes one to two orders lower (mostly a fraction of ~ 1 Jy), deconvolving IRAS data will not reliably resolve our targets (Hawkins 2000). Thus the ISO images appear to be the only ones currently available that can resolve our targets in the far-IR.

3.3. Robustness of Our Results

We consider possibilities that could give a systematic bias to the derived source sizes. To estimate the effects of inaccurate background determination, we decrease and increase the background by 5 %, which is the average background uncertainty, and recalculate the R_{ex} values. While the decrease of the background produces 10–20 % increase in R_{ex} , the increase of the background results in negative F^{ex} values (at central or boundary pixel; a negative F^{ex} implies that the target flux is smaller than the estimated photospheric flux). Thus, while a systematic overestimation of the background, if any, will result in slight underestimation of R_{ex} , considerable underestimation of the background seems unlikely. Moreover, as shown in Table 1 and Figure 1, the uncertainty of the ISO background is only few percent and there exists a good agreement between the ISO and IRAS data without a bias toward a particular observation, which suggests that a systematic over- or underestimation in the ISO background determination is very unlikely. On the other hand, we find that our ‘second calibration’ (dividing the source flux by the background flux pixel-by-pixel) has an effect of increasing R_{ex} values only by $\sim 15\%$.

The estimation of F^* also could be a possible cause of the bias, if any. Here we try two methods for estimating F^* different from the one used in § 3. The first method (method A of Zuckerman et al. 1995) estimates $F^*(12)$ using the empirical relation between $F^*(12)$ and V magnitude as a function of B–V color by Waters, Coté, & Aumann (1987) and extrapolates to $F^*(60)$ and $F^*(90)$ for a blackbody spectrum. The

TABLE 2
COLOR-CORRECTED PHOTOSPHERIC FLUXES
(JY)

Star	$F^{*,cc}$		
	(25)	(60)	(90)
HD 119853	0.393	0.067	0.030
HD 221776	0.845	0.144	0.065
HD 153687	2.280	0.388	0.174
HD 156115	1.481	0.252	0.114
HD 202418	0.399	0.068	0.031
HD 218559	0.594	0.101	0.045
HD 212320	0.216	0.037	0.016
HD 19745	0.049	0.008	0.004
HD 24124	0.056	0.009	0.004
HD 111830	0.095	0.016	0.007
HD 92253	0.129	0.022	0.010
HD 32440	1.331	0.227	0.102

second method (method B of Zuckerman et al. 1995) assumes the IRAS $12\ \mu\text{m}$ flux is photospheric (as in § 3) and extrapolates to $F^*(60)$ and $F^*(90)$ for a blackbody spectrum. The new F^* estimation with methods A and B gives a considerable change in R_{ex} only for HD 156115 and HD 32440, where F^* is more than one-third of the total source flux. These new methods give $\sim 10\%$ larger F^* , and result in 10–20% R_{ex} increase for the above two stars. Thus the method of estimating F^* will not significantly affect the R_{ex} values.

Inaccurate PSF or footprint could also affect our size analysis. As mentioned earlier, we used the model footprint modified for a recent recalibration based on real ISO data from the same C100 camera (Laureijs 1999). Recalculation of R_{ex} with the original model footprint produces a change in the results of less than 20% (the footprint modification resulted in about 50% increase in $r_{mod}(\theta_{ex} = 0)$, or P_c/P_b , but the change in r_{mod} near the r_{obs} values of our targets due to the modification was relatively small). Thus unless the focal plane scale of the true footprint is largely different from that of the adopted footprint, inaccuracy in the adopted footprint is expected not to considerably affect our derived R_{ex} .

4. DISCUSSION

Jura (1999) estimated the extent of the circumstellar material around 8 nearby giants with infrared excess using three source models. Since the models result in sizes that differ from each other by almost an order of magnitude, the size of the infrared excess source may be used to judge which model is most consistent with the observations.

Jura's models require the temperature and radius of the target star (T_* , R_*) and the temperature of the circumstellar grains (T_{ex}). T_* is obtained from the (B–V) color and R_* is inferred from T_* , distance to the star D_* , and V magnitude (see Table 4). Flower's (1996) conversion between (B–V) color and T_* , and the assumption that $M_{bol}(\text{Sun}) = 4.74$ (Bessel, Catelli, & Plez 1998) are used in the above calculation.

To estimate T_{ex} , excess far-IR fluxes at two passbands are fit by $\nu B_\nu(T_{ex})$ for the ejected dust model, and by $B_\nu(T_{ex})$ for the orbiting dust model, where B_ν is the Planck function and ν is the frequency (see Jura 1999). Both IRAS and ISO data were used for the fitting, but we fit the IRAS data ($25\ \mu\text{m}$, $60\ \mu\text{m}$) and the ISO data ($60\ \mu\text{m}$, $90\ \mu\text{m}$) separately because the two

observations have different beam sizes. For the IRAS data, excess fluxes are calculated with assumed photospheric ratios $F^*(25)/F^*(12) = 0.233$ and $F^*(60)/F^*(12) = 0.0371$. For the ISO data, we obtain the excess fluxes by subtracting the photospheric flux calculated in § 3.2 from the total flux. The T_{ex} values derived from the two data sets are each shown in Table 4. We use the average of the two for further analysis.

Jura's estimation for model source sizes are then given by

$$R_{ex} = \begin{cases} 0.5 R_* \left(\frac{T_*}{T_{ex}} \right)^2 & \text{for orbiting dust;} \\ 0.5 R_* \left(\frac{T_*}{T_{ex}} \right)^{2.5} & \text{for ejected dust;} \\ 120 R_* \left(\frac{kT_*}{h\nu} \right)^{2.75} & \text{for cirrus hotspot.} \end{cases} \quad (3)$$

Note that R_{ex} for the cirrus hotspot model is the radius at which half the energy is emitted. Table 5 gives model R_{ex} for our giants obtained by the above equations. Each model results in R_{ex} that differ by an order of magnitude, and only the cirrus model gives R_{ex} dependent on the wavelength.

Orbiting dust and ejected dust model R_{ex} values are to be compared to R_{ex} values derived from observed r_{obs} with an assumption of the shell distribution for the excess emission source, whereas the cirrus hotspot model R_{ex} values are to be compared to those derived with an assumption of the uniform distribution for the excess emission source (see Table 3 for the R_{ex} derived from the observations).

The region of 60 and 90 micron emission in the orbiting dust (Kuiper-belt) model (Table 5) would be spatially unresolved with the C100 detectors. But Table 3 and Figure 2 indicate that the 60 and 90 μm emission regions of our target stars are resolved with typical angular radii $> 20''$. Thus, if the assumption of large (blackbody) grains in the Kuiper-belt is appropriate, then the C100 data imply that the observed far-IR emission is not due to orbiting dust. If particles generated in a Kuiper-belt structure are so small as to not radiate like blackbodies, then the expected far-IR source size could be consistent with the observed sizes. However, as noted by Jura (1999), small particles will be blown out of the systems by radiation pressure and would have to be consistently replenished. Then the dust masses required over the lifetime of the phenomenon would be very large (see Jura 1999).

TABLE 3
OBSERVED AND DERIVED SIZE PARAMETERS

Star	60 μm					90 μm				
	r_{obs}	Shell		Uniform		r_{obs}	Shell		Uniform	
		θ_{ex} (")	R_{ex} (AU)	θ_{ex} (")	R_{ex} (AU)		θ_{ex} (")	R_{ex} (AU)	θ_{ex} (")	R_{ex} (AU)
HD 119853	0.48 ± 0.23	36	4200^{+1000}_{-500}	66	7700^{+14400}_{-1400}	0.74 ± 0.80	30	$3500^{+\infty}_{-1000}$	46	$5300^{+\infty}_{-1700}$
HD 221776	0.62 ± 0.23	33	7000^{+1000}_{-600}	57	12000^{+3800}_{-1700}	0.56 ± 0.32	33	7000^{+2500}_{-1100}	53	11000^{+9100}_{-2200}
HD 153687	0.68 ± 0.19	33	4000^{+400}_{-200}	53	6500^{+1200}_{-700}	0.99 ± 0.72	27	3300^{+2000}_{-800}	39	4800^{+5100}_{-1300}
HD 156115	0.46 ± 0.44	36	$9300^{+\infty}_{-1600}$	71	$18100^{+\infty}_{-5500}$	0.43 ± 0.31	37	9400^{+6900}_{-1700}	62	$15800^{+\infty}_{-4000}$
HD 202418	0.55 ± 0.17	35	7100^{+800}_{-500}	63	12900^{+4100}_{-1600}	0.45 ± 0.19	36	7400^{+1700}_{-900}	60	12300^{+6900}_{-2100}
HD 218559	0.28 ± 0.09	43	7700^{+1200}_{-700}	151	$27100^{+\infty}_{-12200}$	0.28 ± 0.10	43	7700^{+1700}_{-800}	84	$15100^{+\infty}_{-3200}$
HD 212320	0.67 ± 0.41	33	4600^{+1600}_{-500}	56	7900^{+19300}_{-1600}	0.39 ± 0.17	38	5400^{+1200}_{-700}	65	9200^{+7100}_{-1600}
HD 19745	1.89 ± 1.20	24	12200^{+4100}_{-2100}	39	20000^{+21600}_{-5100}
HD 111830	3.07 ± 2.44	20	3200^{+2000}_{-3200}	28	4500^{+5900}_{-4500}	0.84 ± 0.39	29	4500^{+1100}_{-700}	45	7000^{+3000}_{-3100}
HD 92253	1.06 ± 0.52	29	5600^{+1100}_{-600}	48	9200^{+4700}_{-1600}	0.68 ± 0.46	31	6000^{+3200}_{-1100}	50	9600^{+46900}_{-2300}
HD 32440	0.63 ± 0.39	33	7300^{+2700}_{-900}	56	12200^{+30900}_{-2400}	1.51 ± 1.60	22	$4800^{+\infty}_{-2400}$	31	$6800^{+\infty}_{-3600}$

NOTE.—Uncertainties are at 1- σ level. The uncertainty of r_{obs} comes from the source fluxes, F_c and F_b , and the uncertainty of R_{ex} corresponds to that of θ_{ex} which is propagated from r_{obs} . We do not apply our size analysis to 90 μm HD 19745 data because they have negative F_b . HD 24124 is not listed here because the far-IR emission near the star is thought to be due to a galaxy.

TABLE 4
MODEL PARAMETERS

Star	Sp. Type	m_V (mag)	B-V (mag)	D_* (pc)	$ b $ ($^\circ$)	L (L_\odot)	T_* (K)	R_* (10^{12} cm)	$T_{ex,1}$		$T_{ex,2}$	
									IRAS (K)	ISO (K)	IRAS (K)	ISO (K)
HD 119853	G8 III	5.50	0.90	116	48	8.69×10^1	5050	0.85	54	116	47	68
HD 221776	K7 III	6.18	1.59	208	22	4.51×10^2	3800	3.43	87	90	70	59
HD 153687	K4 III	4.82	1.48	123	22	3.86×10^2	4020	2.83	81	141	67	74
HD 156115	K5 III	6.52	1.45	255	13	3.24×10^2	4070	2.53	94	48	75	38
HD 202418	K3 III	6.42	1.41	204	30	2.10×10^2	4140	1.97	77	96	64	61
HD 218559	K4 III	6.43	1.50	179	35	1.95×10^2	3980	2.05	91	76	73	53
HD 212320	G6 III	5.92	1.00	141	50	9.53×10^1	4840	0.97	82	61	67	46
HD 19745	K1 III	9.10	1.05	500	46	6.67×10^1	4770	0.84	148	81	104	55
HD 24124	K1 III	8.45	1.31	505	48	1.69×10^2	4300	1.64	100	...	79	...
HD 111830	K0 III	7.78	1.25	156	15	2.77×10^1	4400	0.63	69	82	58	56
HD 92253	K0 III	7.42	1.19	192	15	5.43×10^1	4500	0.85	65	75	55	53
HD 32440	K4 III	5.47	1.52	218	34	7.39×10^2	3950	4.06	104	66	81	48

NOTE.—This table is similar to Table 1 of Jura (1999). $|b|$ is the absolute galactic latitude, L is the bolometric luminosity, and $T_{ex,1}$ and $T_{ex,2}$ are the grain temperatures for the orbiting dust and the ejected dust models, respectively. The other parameters are defined in the text. HD 153687 (30 Oph) and HD 212320 (HR 8530) are also included in Jura's list. m_V , B-V, and D_* are from the Hipparcos catalog except for HD 19745, for which the magnitudes in the Tycho catalog were adopted and D_* was determined photometrically with $M_V = 0.6$. T_{ex} from the ISO data of HD 24124 is not given because its peak intensity is not on the central pixel.

TABLE 5
MODEL R_{ex} OF TARGET STARS (AU)

Star	Orbiting	Ejected	Cirrus (60)	Cirrus (90)
HD 119853	100	2,100	29,000	88,000
HD 221776	210	3,000	53,000	160,000
HD 153687	120	2,300	51,000	160,000
HD 156115	310	4,200	47,000	140,000
HD 202418	150	2,400	39,000	120,000
HD 218559	150	2,200	36,000	110,000
HD 212320	150	2,200	29,000	89,000
HD 19745	48	780	24,000	74,000
HD 24124	100	1,200	36,000	110,000
HD 111830	72	1,100	15,000	45,000
HD 92253	120	1,800	21,000	64,000
HD 32440	300	4,000	70,000	210,000

Given the substantial uncertainties in the measured ratios for R_{ex} (Table 3), based on the ISOPHOT data, we are unable to choose between the mass ejection and cirrus hotspot models (uncertainties in R_{ex} are asymmetrical and larger toward the positive direction). The reason is that the uncertainties of r_{obs} are substantial, while the difference between values of r_{mod} calculated for these two models is not large. Thus to choose between them one must fall back on the types of arguments given by Jura (1999). Unfortunately, such arguments support neither model particularly well.

Jura (1999) argued against the sporadic dust ejection model for two reasons: (1) a recent ejection of matter would give $F^{ex}(25)$ larger than $F^{ex}(60)$, but no K or late-G giants within 300 pc of the Sun shows $F^{ex}(25) > F^{ex}(60)$; (2) one of the giants with far-IR excess, δ And (HD 3627), is apparently expanding at $v_{cs} \sim 300 \text{ km s}^{-1}$ (Judge, Jordan, & Rowan-Robinson 1987), implying only 20 yr for the dust to reach its estimated R_{ex} ; but none of the stars analyzed by Jura (1999) show significant variability due to the expected dimming of starlight by the dust for the first few months. However, we find that 8 out of 92 giants in the list presented by Zuckerman et al. (1995) have $F^{ex}(25) > F^{ex}(60)$, and such frequency agrees with our simple calculation of $F^{ex}(25) - F^{ex}(60)$ evolution for the detachment of a thin shell, composed of dust with νB_ν emissivity, from the photosphere with a constant expanding velocity. Furthermore, we note that δ And is an unusual K giant. It is classified as a “hybrid star” which possesses both 10^{6-7} K hot corona and cool stellar wind (see Haisch, Schmitt, & Rosso 1992 and references therein), and Judge et al. (1987) suggested that the high velocity wind from δ And may not be responsible for the formation of the circumstellar shell around the star. If the dust shell is assumed to be blown away at v_{cs} comparable to that of the stellar wind of asymptotic giant branch stars (a few tens of km s^{-1}), one would have a much lower possibility of finding significant starlight variability in a given period.

Very recently, Kalas et al. (2000, in preparation) conducted coronagraphic optical observations of 60 Vega-like stars (main-sequence stars with apparent excess far-IR emission), and found reflection nebulae around five stars which resemble those in the Pleiades. This suggests the cirrus hotspot model for the origin

of excess far-IR emission from those five stars. Similar coronagraphic observations for our target stars might help one in choosing between the mass ejection and cirrus hotspot models.

5. SUMMARY

We have analyzed far infrared imaging data of 12 luminosity class III stars with associated dust particles, observed with the C100 camera on *ISO*. Far-IR excess emission is associated with the central star for 11 targets, and the excess emission of only one target appears to be due to a galaxy. Thus we conclude that most of the stars presented by Zuckerman et al. (1995) actually heat dust particles in their vicinity.

Three models for the origin of the circumstellar dust considered by Jura (1999) predict very different source sizes. To estimate the size of the far-IR emission source, we examined the flux ratio of the central to eight boundary pixels of the 3×3 C100 array. In one model considered by Jura (1999), the observed dust is produced as “Kuiper-belt” like materials located within a few hundred AU of the stars are warmed by the increasingly luminous giant star (the orbiting dust model). Such a far-IR emitting region would appear spatially unresolved in the C100 images. But the observed emission regions do appear to be spatially resolved with radius at least a few thousand AU, and possibly significantly larger. With this size uncertainty, we are unable to choose between the other two models discussed by Jura—sporadic mass ejection and interstellar cirrus hotspot. Neither of these models is in particularly good agreement with all existing data (see, e.g., Jura 1999), so a clear choice between them (or other models) awaits additional observations, perhaps with SIRTf.

We are grateful to Carlos Gabriel and Rene Laureijs of the ESA-VILSPA, Nanyao Lu of the IPAC, and Celeste Spangler for helping us with the ISO data analysis. We thank Eric Becklin and Mike Jura for helpful discussion and reading the manuscript. The ISOPHOT data presented in this paper was reduced using PIA, which is a joint development by the ESA Astrophysics Division and the ISOPHOT Consortium. We have used the Simbad database, Aladin sky atlas, and NED skyplot.

REFERENCES

- Bessel, M. S., Catelli, F., & Plez, B. 1998, *A&A*, 333, 231
Flower, P. J. 1996, *ApJ*, 469, 355
Gabriel, C., Acosta-Pabido, J., Heinrichsen, I., Morris, H., & Tai W.-M., 1997, in *ASP Conf. Ser. vol. 125, Astronomical Data Analysis Software and Systems VI*, eds. G. Hunt & H. E. Payne, 108
Haisch, B., Schmitt, J. H. M. M., & Rosso, C. 1992, *ApJ*, 388, L61
Hoffleit, D., & Warren, Jr., W. H. 1991, *The Bright Star Catalogue*, 5th rev. ed. (New Haven: Yale Univ. Obs.)
Houk, N., Cowley, A. P., & Smith-Moore, M. 1975–1988, *Michigan Spectral Catalog*, Vols. 1–4 (Ann Arbor: Univ. of Michigan)
Hawkins, G. W. 2000, private communication
Hawkins, G. W., & Zuckerman, B. 1991, *ApJ*, 374, 227
Judge, P. G., Jordan, C., & Rowan-Robinson, M. 1987, *MNRAS*, 224, 93
Jura, M. 1999, *ApJ*, 515, 706
Leureijs, R. J. 1999, Point spread function fractions related to the ISOPHOT C100 and C200 arrays (http://isowww.estec.esa.nl/users/expl_lib/PHT/c200fpsf02.ps.gz)
Plets, H., Waelkens, C., Oudmaijer, R. D., & Waters, L. B. F. M. 1997, *A&A*, 323, 513
Sopka, R. J., Hildebrand, R., Jaffe, D. T., Gatley, I., Roellig, T., Werner, M., Jura, M., & Zucerkman, B. 1985, *ApJ*, 294, 242
Waters, L. B. F. M., Coté, J., & Aumann, H. H. 1987, *A&A*, 172, 225
Zuckerman, B., Kim, S. S., & Liu, T. 1995, *ApJ*, 446, L79